JGR

RESEARCH ARTICLE

Correspondence to:
G. Chisham,
gchi@bas.ac.uk

Magnetic local time variation and scaling of poleward auroral boundary dynamics

N. Longden[1], G. Chisham[1], and M. P. Freeman[1]

[1]British Antarctic Survey, Cambridge, UK

Abstract The balance of dayside and nightside reconnection processes within the Earth's magnetosphere and its effect on the amount of open magnetic flux threading the ionosphere is well understood in terms of the expanding-contracting polar cap model. However, the nature and character of the consequential fluctuations in the polar cap boundary are poorly understood. By using the poleward auroral luminosity boundary (PALB), as measured by the FUV instrument of the IMAGE spacecraft, as a proxy for the polar cap boundary, we have studied the motion of this boundary for more than 2 years across the complete range of magnetic local time. Our results show that the dayside PALB dynamics are broadly self-similar on timescales of 12 min to 6 h and appear to be monofractal. Similarity with the characteristics of solar wind and interplanetary magnetic field variability suggests that this dayside monofractal behavior is predominantly inherited from the solar wind via the reconnection process. The nightside PALB dynamics exhibit scale-free behavior at intermediate time scales (12–90 min) and appear to be multifractal. We propose that this character is a result of the intermittent multifractal structure of magnetotail reconnection.

1. Introduction

Magnetic reconnection is a universal physical process that occurs in magnetized plasmas throughout the heliosphere and beyond, involving a change in the connectivity of magnetic field lines which changes the overall topology of the magnetic field. Magnetic reconnection between the interplanetary magnetic field (IMF) and the Earth's magnetic field occurs at the Earth's magnetopause and is the main mechanism for the transfer of mass, energy, and momentum from the solar wind into the Earth's magnetosphere. This reconnection typically alters the topology of the magnetosphere, changing some magnetic field lines from a "closed" type, with both ends intersecting the Earth, to an "open" type, with one end connected to the IMF. This leads to an expansion of the polar cap—the enclosed dark region of the ionosphere poleward of the auroral oval—that almost exclusively contains open magnetic flux. Some of the open flux is ultimately reclosed by reconnection in the magnetotail, which is related to substorm activity [e.g., *Milan et al.*, 2007; *Chisham et al.*, 2008, and references therein], driving contraction of the ionospheric polar cap. The boundary between the open magnetic flux in the polar cap and the closed magnetic flux of the auroral zone of the ionosphere is termed the open-closed magnetic field line boundary (OCB).

Magnetopause reconnection can occur for all orientations of the IMF but its global rate maximizes when the orientation of the IMF is southward, antiparallel to the geomagnetic dipole [e.g., *Chisham et al.*, 2008; *Fuselier et al.*, 2002, and references therein]. The orientation of the IMF affects the location of magnetopause reconnection, with reconnection at low latitudes during periods dominated by southward IMF and reconnection at higher latitudes during periods dominated by northward IMF [e.g., *Chisham et al.*, 2008].

Typically, reconnection at the magnetopause and in the magnetotail occurs between open and closed magnetic field lines and so the OCB is colocated with the reconnection site [e.g., *Chisham et al.*, 2008]. However, during predominantly northward IMF, magnetopause reconnection can occur between the IMF and already open field lines and does not produce any additional open flux in the magnetosphere [*Chisham et al.*, 2004; *Milan et al.*, 2008]. In this case, the magnetopause reconnection site and its ionospheric projection are located poleward of the OCB [e.g., *Chisham et al.*, 2008]. Similarly, immediately after substorm onset, magnetotail reconnection typically initially involves closed magnetic field lines, forming a plasmoid but without closing open magnetic flux. In this case, the reconnection site projects to a location in the ionosphere

equatorward of the OCB until reconnection between open magnetic field lines takes over, corresponding to plasmoid ejection [*Freeman et al.*, 2007].

Reconnection is a relatively localized process in the magnetosphere [e.g., *Borovsky*, 2008] and dayside and nightside reconnection are largely independent [e.g., *Milan et al.*, 2008]. However, the global net rate of reconnection can be estimated from the rate of change of the polar cap area [e.g., *Milan et al.*, 2003; *Chisham et al.*, 2008]. Hence, the global motion of the OCB can be used as a proxy measure of the balance between dayside (expanding polar cap) and nightside (contracting polar cap) reconnection, during most conditions.

A number of techniques exist to estimate the location of the OCB and, hence, track the net reconnection rate in the magnetosphere. The most reliable proxies for the location of the OCB are considered to be particle precipitation boundaries measured by satellites in low-altitude orbits, such as those of the Defense Mete-orological Satellites Program [e.g., *Vampola*, 1971; *Makita et al.*, 1983; *Makita and Meng*, 1984; *Newell et al.*, 1991; *Mishin et al.*, 1992; *Newell et al.*, 1996; *Sotirelis and Newell*, 2000]. However, these yield only two-point measurements of the OCB in each hemisphere in each 100 min orbit of the satellite, making these instruments unsuitable for tracking the detailed motion of the OCB. Many other instruments have been used to provide estimates of the location of the OCB at higher spatial and temporal resolutions. These instruments include HF radars [e.g., *Baker et al.*, 1995, 1997; *Milan et al.*, 1999; *Milan and Lester*, 2001; *Chisham et al.*, 2001, 2002; *Chisham and Freeman*, 2003], ground-based magnetometers [e.g., *Iijima and Potemra*, 1978; *Mishin*, 1990], all-sky cameras [e.g., *Akasofu and Kimball*, 1965; *Feldstein and Galperin*, 1985], meridian-scanning pho-tometers [e.g., *Blanchard et al.*, 1995; *Sandholt et al.*, 1998], and satellite-based imagers [e.g., *Brittnacher et al.*, 1999; *Kauristie et al.*, 1999; *Baker et al.*, 2000; *Carbary et al.*, 2003; *Boakes et al.*, 2008; *Longden et al.*, 2010].

The poleward auroral luminosity boundary (PALB) derived from satellite images has been shown to be a good proxy for the location of the OCB, once corrections have been applied dependent on imager type and magnetic local time (MLT) [e.g., *Carbary et al.*, 2003; *Boakes et al.*, 2008; *Longden et al.*, 2010]. Specifically, in the predawn MLT sector, boundaries determined from imagers sensitive to proton auroral emissions are typ-ically located further poleward than those determined from electron auroral emissions and are hence closer to the OCB, whereas the opposite applies in the dusk and premidnight MLT sectors [e.g., *Wild et al.*, 2004; *Boakes et al.*, 2008; *Longden et al.*, 2010]. Additionally, during magnetopause reconnection under northward IMF conditions a bright spot of proton auroral emissions can often be observed poleward of the main auro-ral oval around noon MLT [e.g., *Milan et al.*, 2000; *Frey et al.*, 2002; *Fuselier et al.*, 2002]. After taking these factors into account, PALBs can provide continuous and complete spatial coverage of the OCB (in a sin-gle hemisphere) at high (∼2 min) temporal resolution for long (∼10 h) intervals, making them suitable for use in large-scale studies of OCB behavior and hence of reconnection across a wide range of temporal and spatial scales.

A number of studies have identified scale-free dynamics in fluctuations in the magnetosphere-ionosphere (M-I) system, such that there is no observable temporal or spatial scale on which these fluctuations pref-erentially occur. Phenomena exhibiting scale-free characteristics include ground-based magnetic field perturbations [e.g., *Vörös et al.*, 1998], auroral and polar cap indices [e.g., *Takalo et al.*, 1993; *Takalo and Timonen*, 1994; *Takalo et al.*, 1994, 1995; *Takalo and Timonen*, 1998; *Hnat et al.*, 2003, 2005], the *SYM-H* and *Dst* indices [e.g., *Takalo et al.*, 1995; *Wanliss*, 2005], auroral perturbations [e.g., *Uritsky et al.*, 2002; *Kozelov et al.*, 2004; *Uritsky et al.*, 2008; *Vallières-Nollet et al.*, 2010], and ionospheric convection velocity [e.g., *Abel et al.*, 2006; *Parkinson*, 2006; *Abel et al.*, 2007, 2009].

Scale-free dynamics have also been observed in the solar wind and IMF [e.g., *Hnat et al.*, 2003, 2005; *Parkinson*, 2006]. Hence, there has been much discussion as to whether the scale-free dynamics observed within the M-I system are intrinsic or are inherited through reconnection with the solar wind and IMF [e.g., *Freeman et al.*, 2000; *Uritsky et al.*, 2002; *Watkins*, 2002; *Uritsky et al.*, 2008]. Much of the comparison between the M-I system behavior and that of the solar wind has been performed using geomagnetic and auro-ral indices or auroral emission events [e.g., *Freeman et al.*, 2000; *Uritsky et al.*, 2001; *Hnat et al.*, 2003, 2005; *Wanliss*, 2005], which did not allow for the distinction of different behavior in different MLT regions or the separation of behavior driven by reconnection with the IMF from that within the magnetotail. However, studies of ionospheric convection have highlighted differences in the scaling of velocity fluctuations in the nightside and dayside ionosphere [*Abel et al.*, 2006; *Parkinson*, 2006]. *Parkinson* [2006] observed that the fluctuations in velocity around local noon most reflected the trends of the solar wind and appeared to be monofractal. Monofractal processes have scale-invariant properties that can be characterized by a single

scaling exponent (or fractal dimension) throughout the entire signal. In addition, *Parkinson* [2006] observed that the velocity fluctuations in the midnight sector of the ionosphere exhibited multifractality. This is consistent with the multifractal nature of the magnetotail, as determined from in situ spacecraft observations [*Lui*, 2001; *Vörös et al.*, 2003]. Multifractal processes are more complex than monofractal processes, in that a single scaling exponent is not sufficient to describe their dynamics; instead, a continuous spectrum of exponents is needed. Multifractal processes can generally be decomposed into many subsets characterized by different exponents and are very common in nature, especially in geophysics.

To identify scaling behavior in the dynamics of the M-I system across all MLT sectors in response to magnetic reconnection, we present the results of a detailed analysis of temporal fluctuations in the PALBs derived from IMAGE FUV images. We consider the PALB dynamics in twenty-four 1 h MLT sectors to investigate the characteristic differences in behavior throughout the system. We also assess whether the dynamics in each MLT sector appear to be monofractal or multifractal and consider both poleward and equatorward motion of the PALB separately.

2. Instrumentation and Method

2.1. Instrumentation and Data Sets

The auroral boundaries are derived from auroral images taken by the FUV instrument on board the IMAGE satellite during the period of May 2000 to August 2002. During this interval the satellite apogee was close to the North Pole; hence, all the images were of the Northern Hemisphere polar region. The FUV instrument is composed of three detectors; the Wideband Imaging Camera (WIC) and two Spectrographic Imagers (SI12 and SI13) [*Mende et al.*, 2000a]. WIC is sensitive to auroral emissions in the 140 to 190 nm range of the N_2 Lyman-Birge-Hopfield band [*Mende et al.*, 2000a, 2000b]. SI12 is sensitive to Doppler-shifted Lyman-α emissions in the 121.8 nm band, stimulated by proton precipitation, and SI13 is sensitive to the 135.6 nm oxygen emission band, stimulated by energetic electron precipitation [*Mende et al.*, 2000a, 2000c]. The IMAGE FUV data set has a time resolution of approximately 2 min [*Burch*, 2000].

The technique used to derive the auroral boundaries is outlined in detail in *Longden et al.* [2010]. In this technique, each auroral image is divided into 24 sections, each covering a 1 h sector of MLT. For each MLT sector, latitudinal profiles of auroral luminosity are generated and modeled as either a single or double Gaussian function, depending on which is the more suitable model. The poleward and equatorward boundaries of auroral luminosity are estimated from these models for each MLT sector. Over 2 million poleward auroral luminosity boundaries (PALB) have been estimated from images from each FUV detector, providing separate estimates for proton and electron auroral boundaries. Figure 1a shows the auroral luminosity recorded by the SI12 detector at ∼03:28 UT on 4 November 2000 as an example illustration of the results of the technique. The derived PALBs (with latitudinal offset corrections applied [see *Longden et al.*, 2010]) are indicated by white diamonds. The white curve shows a linear interpolation across successfully located boundaries. Figure 1b shows the evolution of auroral luminosity intensity over a 6 h period, between 00:00 and 06:00 UT on 4 November, for the 00 to 01 MLT sector (the highlighted MLT sector in Figure 1a). White squares denote the PALBs with error bars showing the uncertainties of each boundary.

2.2. Methodology

Structure function analysis is a well-established method used to study scaling and self-similarity in data sets. Specifically, the structure function describes how the moments of absolute differences between samples in a data set vary as a function of separation and can be used to identify scale-free behavior in fluctuations. We calculate the first six moments of the structure function S for differences in the latitude of the PALB, $\lambda(t)$, with respect to the temporal separation, τ, following

$$S_m(\tau) = < |\delta\lambda(t_i, \tau)|^m > \tag{1}$$
$$\delta\lambda(t_i, \tau) = \lambda(t_i + \tau) - \lambda(t_i)$$

where m is the moment (or order) of the structure function, t_i is the timestamp of boundary i, $<>$ denotes the ensemble average over all points $i = 1, ..., N$, and τ is an integer multiple of $\Delta t = 2$ min, which is the closest integer number of minutes to the time resolution of the boundary data set (typically ∼122.8 s). We calculate the structure functions for time separations of 2 to 360 min for each 1 h MLT sector. We additionally calculate these structure functions separately for poleward PALB motions and equatorward PALB motions to
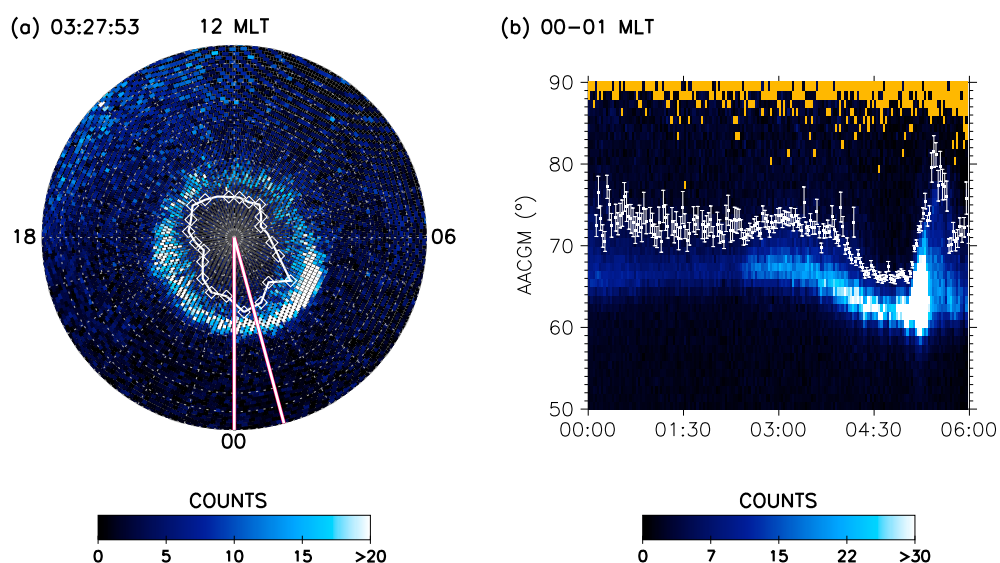
Figure 1. (a) FUV intensity image of the Northern Hemisphere observed by the IMAGE FUV SI12 instrument at 03:28 UT 4 November 2000 in Altitude Adjusted Corrected Geomagnetic Coordinates with a lowest latitude of 40°. The solid white lines mark the 00:00–01:00 MLT sector. White diamonds denote the poleward auroral boundaries derived using the technique of *Longden et al.* [2010]. The white curve indicates a linear interpolation between successfully located boundaries. (b) Intensity counts between 00:00 and 06:00 UT in the 00:00–01:00 MLT sector. White squares indicate the derived poleward auroral luminosity boundaries, with error bars showing the uncertainties in the boundary location estimates. Undeterminable and zero count intensities are shown in yellow. All count values above 20 in Figure 1a and 30 in Figure 1b have been saturated.

preserve information about the direction of the boundary motion and, hence, about contraction and expansion of the polar cap. The auroral boundary data sets used to construct the structure functions have been conditioned to remove all boundary differences greater than the 8σ level of the difference distributions. This reduces the impact of the inadequate sampling of unlikely but extreme events when calculating the higher-order structure functions [e.g., *Hnat et al.*, 2005; *Abel et al.*, 2007, 2009].

Fractal, or scale-free, behavior is indicated when a structure function appears as a straight line in a log-log plot of the structure function (S) against the time separation (τ), such that the structure function is proportional to some power ζ of the time separation [e.g., *Hnat et al.*, 2003; *Abel et al.*, 2007]:

$$S_m(\tau) \propto \tau^{\zeta(m)}$$

$$\log S_m(\tau) = \zeta(m) \log \tau + C$$

(2)

Variation in the scaling of structure functions (i.e., in $\zeta(m)$) with respect to the order (m) can help to discriminate between monofractal and multifractal scaling. When the exponent ζ is linearly proportional to the moment m, i.e., $\zeta(m) \propto m\zeta(1)$, then the boundary motion is self-similar, or monofractal, i.e., fluctuations in the boundary motion are characterized by a single scaling exponent. In the alternative case, the boundary motion is scale free but the fluctuations in the boundary motion cannot be characterized by a single scaling exponent, in which case we refer to the boundary motion as multifractal, indicated by a nonlinear, approximately quadratic, $\zeta(m)$ variation with m [e.g., *Chapman et al.*, 2005; *Hnat et al.*, 2007]. In this paper, we fit a quadratic function to the $\zeta(m)$ variation with m to discriminate between potential monofractality and multifractality.

For illustration, the first-order structure function calculated for all auroral boundary motion, both poleward and equatorward, in all 24 MLT sectors combined, for PALBs derived from SI12 images, is shown as the diamond symbols in Figure 2. The structure function appears to contain three distinct regions, with breaks in its slope at ~12 min and ~90 min, indicated by the vertical dotted lines. In the central region, the structure function is approximately a power law with exponent 0.281 ± 0.003, as indicated by the best linear least squares fit to the structure function covering this range (i.e., 12 to 90 min) shown by the solid line in Figure 2. Small deviations from the local trend in the structure function are caused by reduced numbers of boundary locations for particular time separations (e.g., at $\tau = 44$ min). The structure functions for all PALB motion in
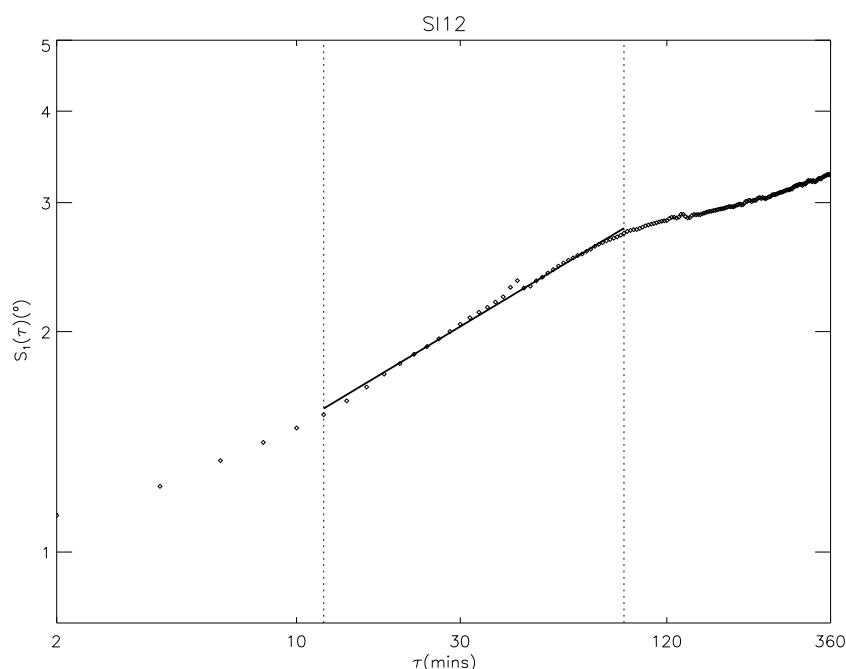
Figure 2. The first-order temporal structure function ($S_1(\tau)$) of PALB locations derived from the IMAGE SI12 instrument between 2000 and 2002 (black diamond symbols) as a function of time separation τ. Boundary motions from all 24 MLT sectors and both poleward (positive) and equatorward (negative) motions are included in the calculation of the structure function. The best linear least squares fit to the structure function in the interval 12 to 90 min is also shown (black solid curve). This time separation range is delimited by the vertical black dashed lines. Both axes have a logarithmic scale.

all MLT sectors for boundaries derived from SI13 and WIC images (not shown) follow the same trend exhibited in the SI12 boundary fluctuations, with a change in the scaling at low (<12 min) and high (>90 min) time separations. Data relating to SI12 boundaries is presented here as SI12 images are less susceptible to dayglow contamination than the WIC and SI13 instruments (see *Longden et al.* [2010] for further details).

3. Results

Figure 3 shows the first-order ($m = 1$) structure function for PALB locations derived from SI12 images separated by MLT sector. Both poleward and equatorward PALB motions have been included in the calculation of the structure functions shown in this figure. Inset are the variations of the structure functions with MLT for τ values of 2, 30, and 360 min. The surface shows the variation in the character of the structure function with time separation, as is evident in Figure 2, as well as the variations with MLT. For low τ values (i.e., $\tau = 2$ and 30 min), small troughs in the structure function are evident in the postdawn and predusk sectors ($\sim$06 to 10 MLT and $\sim$14 to 18 MLT, respectively, for $\tau = 30$ min). At higher τ values, these troughs become less apparent and peaks in the structure function are evident around local dawn and noon ($\sim$04 to 07 and $\sim$09 to 14 MLT respectively for $\tau = 360$ min), with elevated values continuing into the dusk sector (until $\sim$ 20 MLT). On the nightside ($\sim$21 to 03 MLT), the structure function values are largely consistent across the MLT sectors for all τ values.

Similar trends are evident in the first-order structure function for PALB locations derived from SI13 images (not shown), although the postdawn and predusk troughs are evident for all τ values across the complete 2 to 360 min range. At high τ values, peaks around local dawn, noon, and dusk are clear ($\sim$05 to 08, $\sim$10 to 12, and $\sim$18 to 20 MLT, respectively, for $\tau = 360$ min), with separation between the noon and dusk peaks that is lacking in the SI12 PALB location structure function. The noon peak is also less dominant than the peaks around local dawn and dusk, in contrast to the SI12 PALB location structure function. The first-order structure function for PALB locations derived from WIC images (also not shown) is similar to that for SI13 PALBs for τ values exceeding $\sim$16 min. At lower time separations, the postdawn and predusk troughs, while evident in the structure function separating the dawn, noon, and dusk peaks, exceed the structure function values in the nightside MLT sector. It should be noted that PALBs derived from WIC images in the MLT
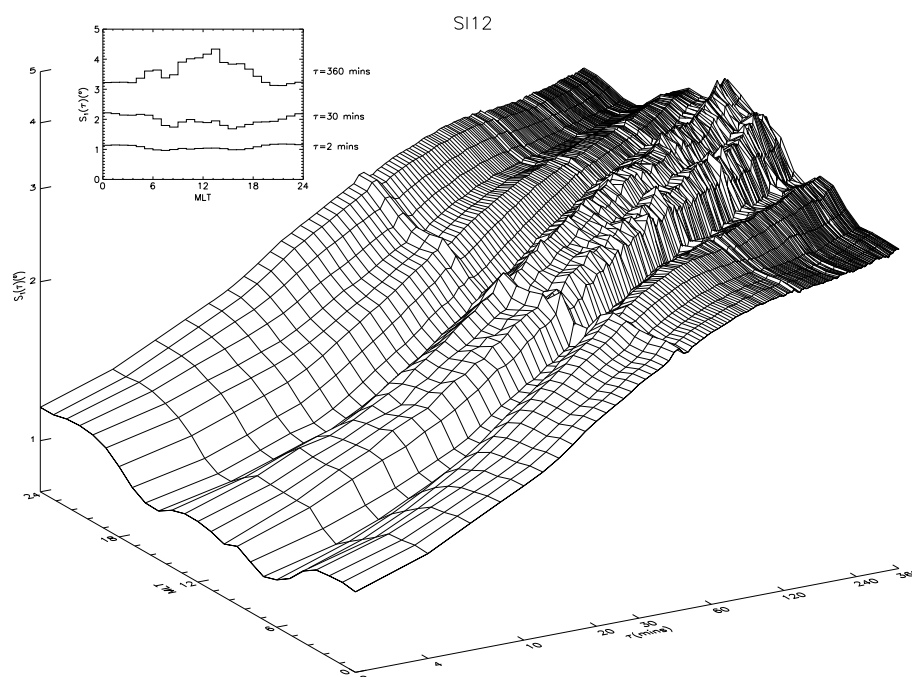
Figure 3. Surface plot of the first-order temporal structure function ($S_1(\tau)$) of PALB locations derived from the IMAGE SI12 instrument in twenty-four 1 h MLT sectors (bottom left scale). Time separations (τ) and $S_1(\tau)$ axes have a logarithmic scale. Both poleward (positive) and equatorward (negative) motions of the auroral boundary are included in the structure function analysis. The inset shows the first-order structure functions of the PALBs by MLT for selected τ values.

sectors around local noon are considered to be less reliable than those from SI12 and SI13 because of dayglow contamination [*Longden et al.*, 2010].

Figure 4 shows the first-order structure functions for PALB locations derived from SI12 images for each of the twenty-four 1 h MLT sectors, with the structure functions for poleward (black curves) and equatorward (red curves) PALB motion shown separately. Vertical dashed black lines delimit the 12 to 90 min time separation region in each panel. It is between these two time separations that there is evidence of scaling (i.e., straight line structure functions on the log-log plots) at all MLTs. Hence, most of the results section focuses on the structure functions in this region. The origin of the scaling breaks at 12 and 90 min are explored further in the discussion section.

The number of PALB location differences used in the calculation of the structure functions in Figure 4, for each time separation, are shown in Figure 5. Fewer auroral boundaries are generally derived in the dayside MLT sectors than in the nightside MLT sectors when using the automated boundary location technique. This is predominantly the result of the effects of low-intensity auroral emissions in the dayside ionosphere and contamination of WIC and SI13 images with dayglow emissions (see *Longden et al.* [2010] for further details). Low numbers of PALBs at particular time separations (e.g., $\tau = 44$ min) are also evident. This is a result of the IMAGE FUV sampling interval being a noninteger number of minutes (typically ~122.8 s). This results in the small deviation in the scaling trend seen in the structure functions (e.g., in Figure 4).

In Figure 4, there is a clear flattening of the slope of the structure functions in the nightside MLT sectors (~21 to 03 MLT) for time separations greater than ~90 min, for both poleward and equatorward PALB motion. At intermediate time separations ($12 \leq \tau \leq 90$ min), the structure functions of poleward PALB motion (black) are consistently greater than those for equatorward PALB motion (red) on the nightside, with little difference at longer and shorter time separations.

The scaling break at short time scales ($\tau < 12$ min) is less pronounced around local midnight than on the dayside, particularly for poleward PALB motion. The structure functions for poleward PALB motion derived from SI12 images are shown on their own in Figure 6. The best linear least squares fit to the structure functions in the 12 to 90 min time separation range are indicated by the blue dashed lines, highlighting this deviation on the shorter time scales.
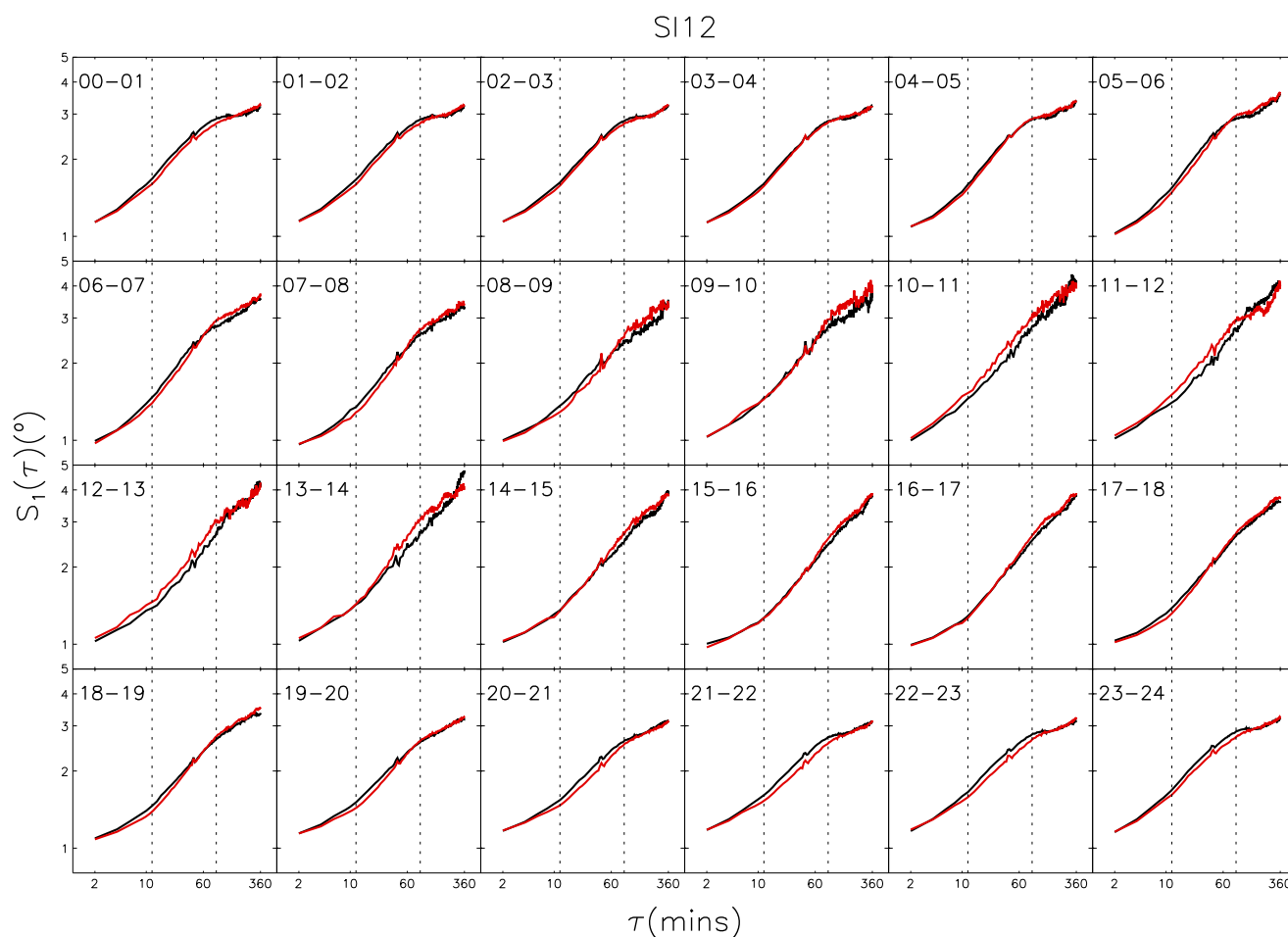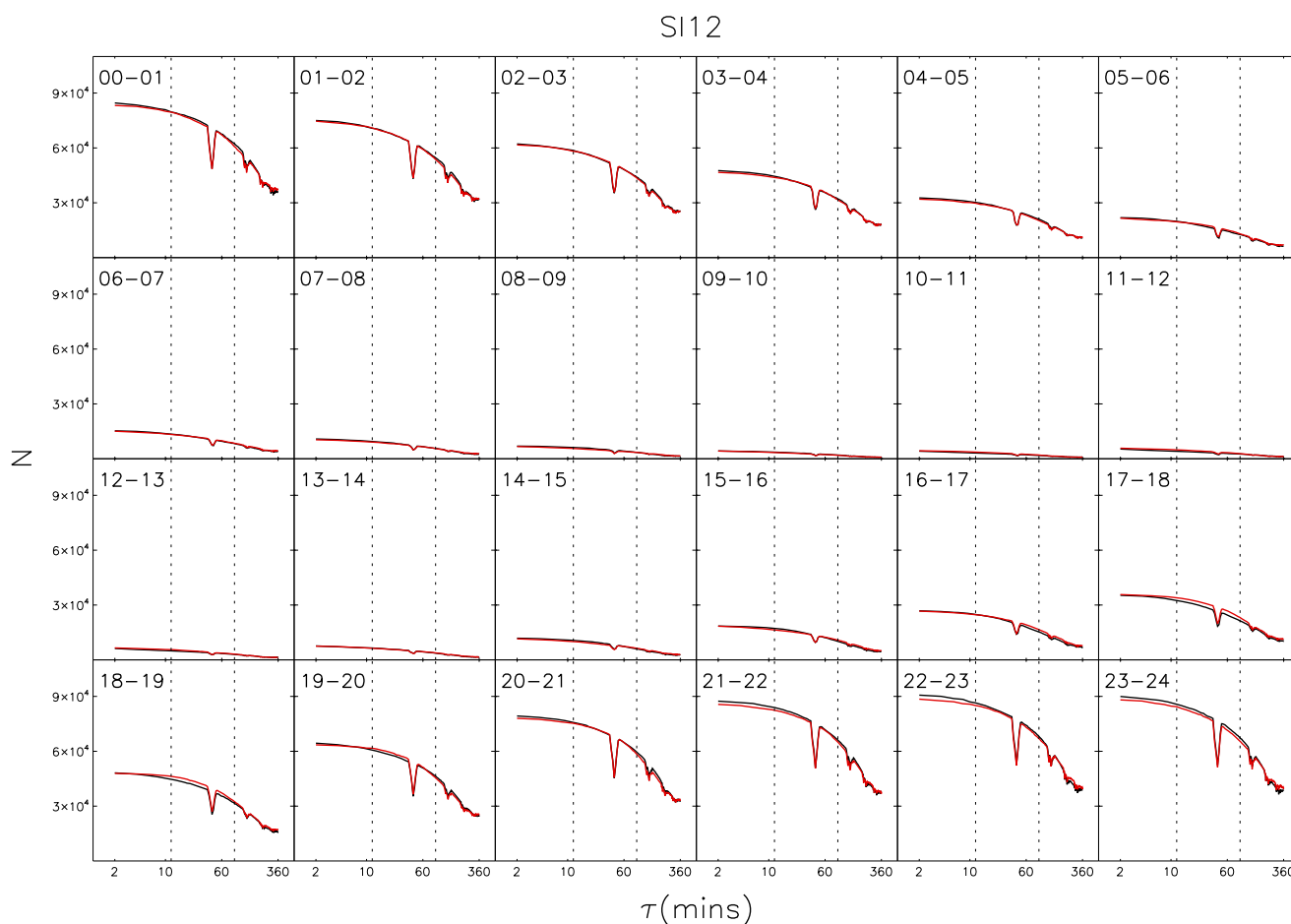
Figure 4. The first-order temporal structure function ($S_1(\tau)$) of PALB locations derived from the IMAGE SI12 instrument in twenty-four 1 h MLT sectors. Both axes have a logarithmic scale. Structure functions for poleward (positive) boundary motions are shown by the black curves and those for equatorward (negative) boundary motions are shown by red curves. Vertical dashed black lines indicate the 12 to 90 min time separation range.

On the dayside (∼09 to 15 MLT), the structure functions shown in Figure 4 do not exhibit much evidence of the scaling break at $\tau \geq 90$ min. The structure functions for equatorward PALB motion (red) typically exceed those for poleward PALB motion (black) across all time separations while there is some evidence of a break in scaling at $\tau \approx 12$ min, especially in the later MLT sectors. In some dayside MLT sectors, the structure function appears to be more irregular than on the nightside, which we attribute to the smaller number of successfully located PALBs (see Figure 5).

The structure functions in the dawn (∼03 to 09 MLT) and dusk (∼15 to 21 MLT) sectors show a transition between the dayside and nightside trends such that the difference between the poleward and equatorward PALB motion structure functions minimizes near dawn and dusk and the scaling break at $\tau \approx 90$ min becomes less pronounced moving from night to day. The scaling break at shorter time scales ($\tau \approx 12$ min) is more apparent at dusk than at dawn.

The structure functions for the motion of PALBs derived from SI13 and WIC images (not shown) exhibit similar trends to those from SI12 PALBs, although the differences between the poleward and equatorward PALB motion structure functions in the intermediate region ($12 \leq \tau \leq 90$ min) are more pronounced in the nightside sectors for SI13.

The higher-order moments ($m = 2$ to 6) of the structure functions of the SI12 PALB poleward (black) and equatorward (red) motion are shown in Figure 7 in addition to the first-order structure function. In each panel, the lowest curves are the first-order structure functions $S_1(\tau)$, as shown already in Figure 4 with the higher-order structure functions increasing up the panel. Figure 8 shows the variation of slopes ($\zeta(m)$) of
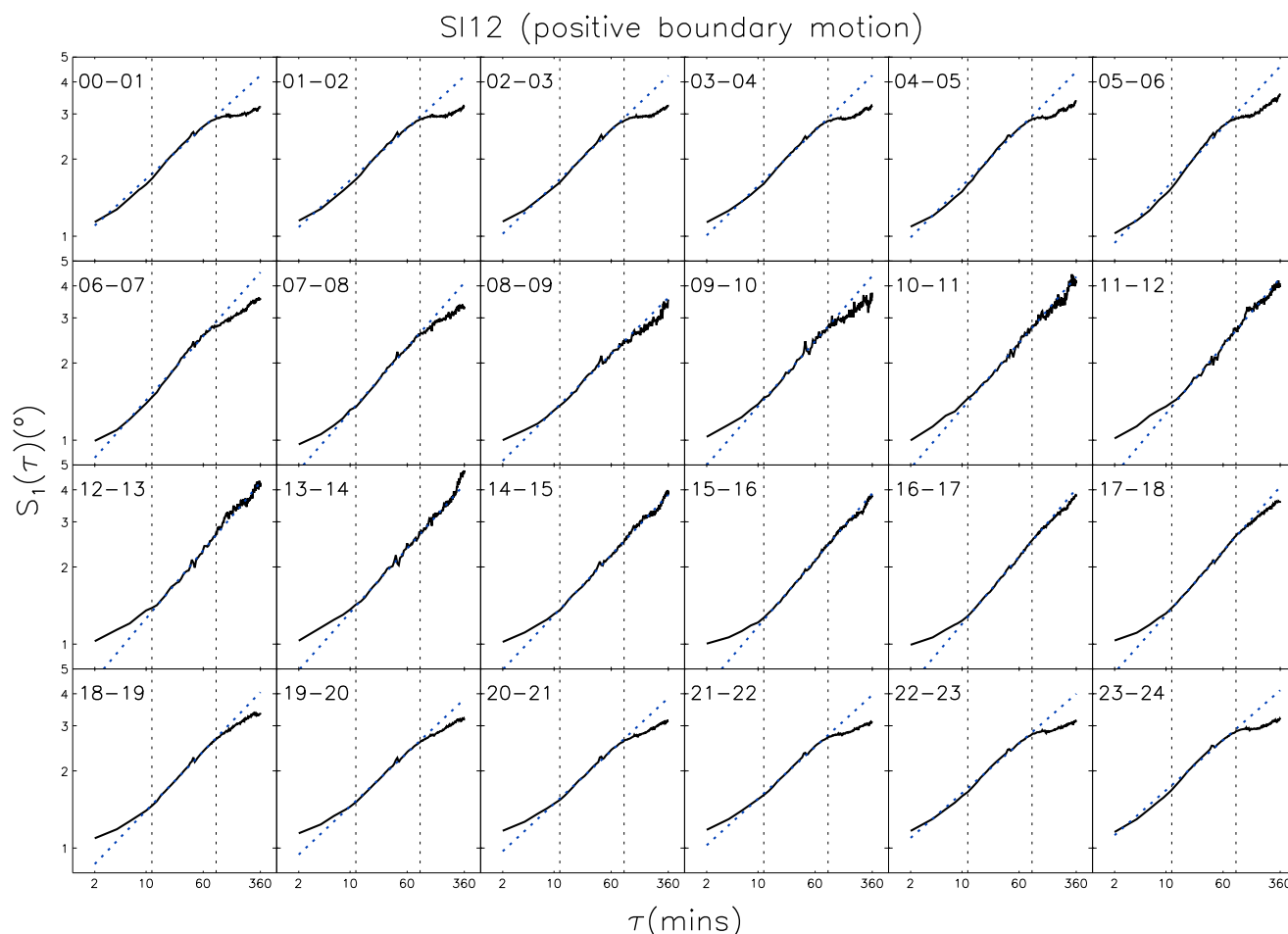
Figure 5. The number of PALB locations derived from the IMAGE SI12 instrument used to calculate the first-order temporal structure function ($S_1(\tau)$) in twenty-four 1 h MLT sectors. Poleward (positive) boundary motion numbers are shown by the black curves and those for equatorward (negative) boundary motion are shown by red curves. The time separation (τ) axis has a logarithmic scale. Vertical dashed black lines indicate the 12 to 90 min time separation range.

the linear fits to the structure functions with the moment, m, for each MLT sector. Black diamond symbols indicate $\zeta(m)$ for the structure functions of poleward PALB motion, while red diamond symbols are the $\zeta(m)$ relating to equatorward PALB motion. $\zeta(0) = 0$ (by definition) is also included in each panel. The best least squares quadratic fit to each ζ function (of the form $\zeta = am^2 + bm$) is also shown in Figure 8 by the solid lines. Error bars on the diamond symbols indicate the 95% confidence interval on the linear fits to the structure functions in the τ range of 12 to 90 min (i.e., the fits to the structure functions shown in Figure 7). The 95% confidence interval of the linear fits to these structure functions are greatest in dayside MLT sectors, consistent with greater irregularity around local noon resulting from the reduced amount of data, as is clearly evident in Figure 7.

In the nightside MLT sectors (~21 to 03 MLT), the ζ functions for poleward and equatorward motion are broadly similar, with $\zeta(m)$ for poleward PALB motion (black) slightly exceeding that for equatorward PALB motion (red), and both are nonlinear. This nonlinearity implies multifractal characteristics (i.e., multiple scaling exponents). On the dayside (~09 to 15 MLT), the ζ function for equatorward motion (red) exceeds that for poleward motion (black) for all moments and is approximately linear, implying monofractality (i.e., single scaling exponent). As with the structure functions variations, the ζ function variations seen at dawn (~03 to 09 MLT) and dusk (~15 to 21 MLT) exhibit a transition from the linear, monofractal regime seen on the dayside to the nonlinear, multifractal regime seen on the nightside. The ζ functions for structure functions of SI13 PALB motion follow similar trends (not shown). Those for WIC PALB motion (also not shown) appear to be consistently less linear, with only the ζ functions for equatorward PALB motion around noon showing evidence of linearity.
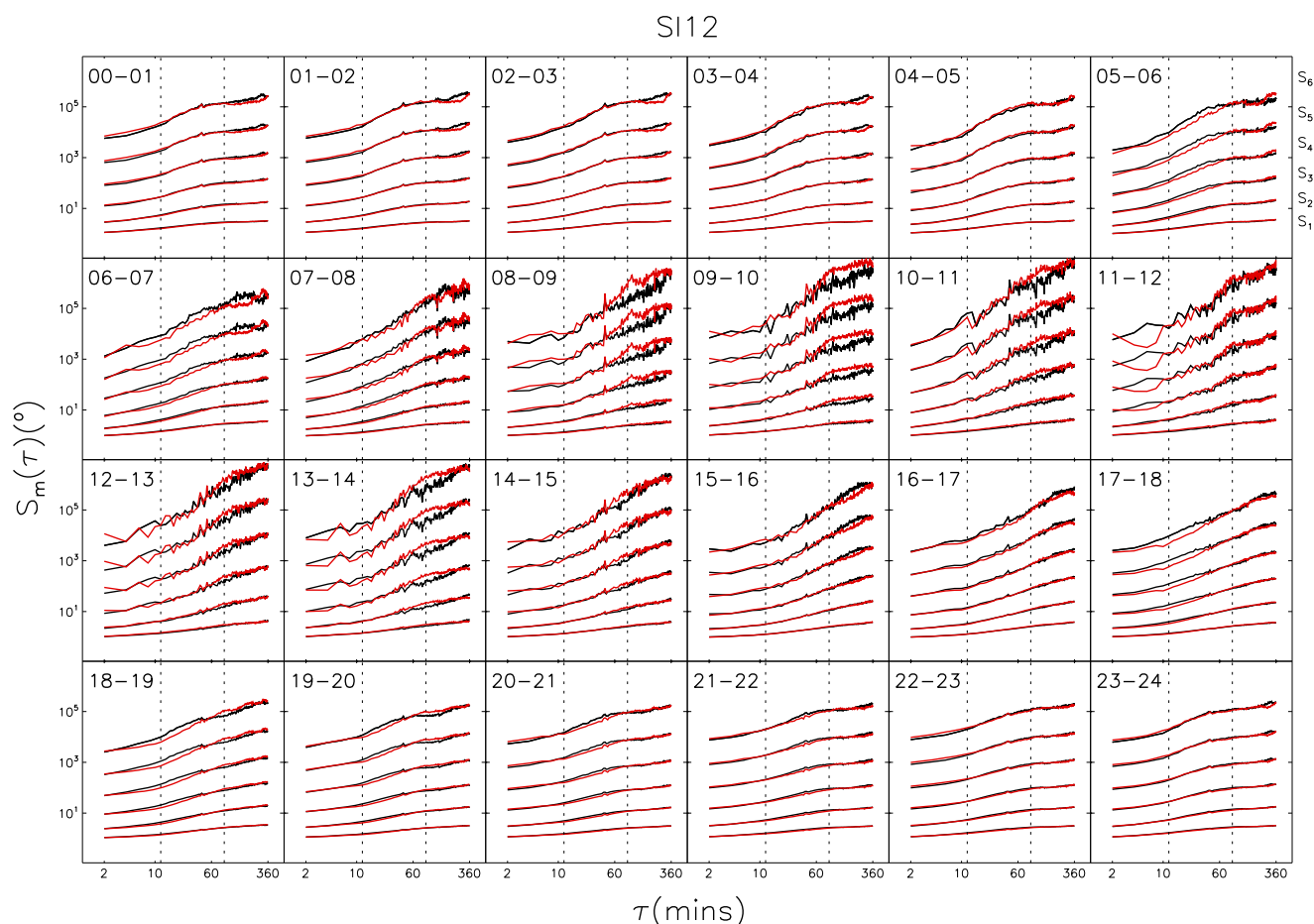
Figure 6. The first-order temporal structure function ($S_1(\tau)$) of PALB locations derived from the IMAGE SI12 instrument in twenty-four 1 h MLT sectors. Both axes have a logarithmic scale. Structure functions for poleward (positive) boundary motions are shown by the black curves. The best linear least squares fit to the structure function in the 12 to 90 min time separation range are shown by the dashed blue lines. Vertical dashed black lines indicate the 12 to 90 min time separation range.

Figure 9 shows the linear (a, c, and e) and quadratic (b, d, and f) coefficients of the quadratic functional fits to the ζ functions for SI12 (as shown in Figure 8), SI13, and WIC PALBs, respectively. Coefficients for the fits to the ζ functions for poleward PALB motion are indicated by black curves with square symbols while those for equatorward PALB motion are indicated by red curves with square symbols. Error bars on the squares indicate the 95% confidence intervals of the fit to the ζ functions. The slopes of the first-order structure functions for the solar wind ϵ parameter given by *Hnat et al.* [2005] for solar maximum (2000 to 2001, solid grey shading) and by *Parkinson et al.* [2007] for 2000, 2001, and 2002 (dotted, dashed, and dash-dotted lines, respectively) are indicated in the panels showing the linear fit coefficients (Figures 9a, 9c, and 9e).

4. Discussion

The structure and ζ functions for the PALB motion (Figures 4 and 8) highlight the differences between the dayside and nightside auroral boundary dynamics. The dayside PALB dynamics are broadly self-similar on time scales of 12 min to 6 h and appear to be monofractal. On the nightside, while scale-free behavior is observed at intermediate time scales ($12 \leq \tau \leq 90$ min), there is clear evidence of a scaling break at time separations of ~ 90 min, and the dynamics are suggestive of multifractality.

The scaling break at $\tau \approx 90$ min seen on the nightside is broadly consistent with measurements of the fluctuations of the geomagnetic indices *AE*, *AU*, and *AL* [*Takalo et al.*, 1993; *Takalo and Timonen*, 1994; *Hnat et al.*, 2003, 2005], which show a scaling break close to a time separation of 2 h. When fluctuations of the PALB in all MLT sectors are considered (Figure 2), the break in scaling close to this time scale is clear and the
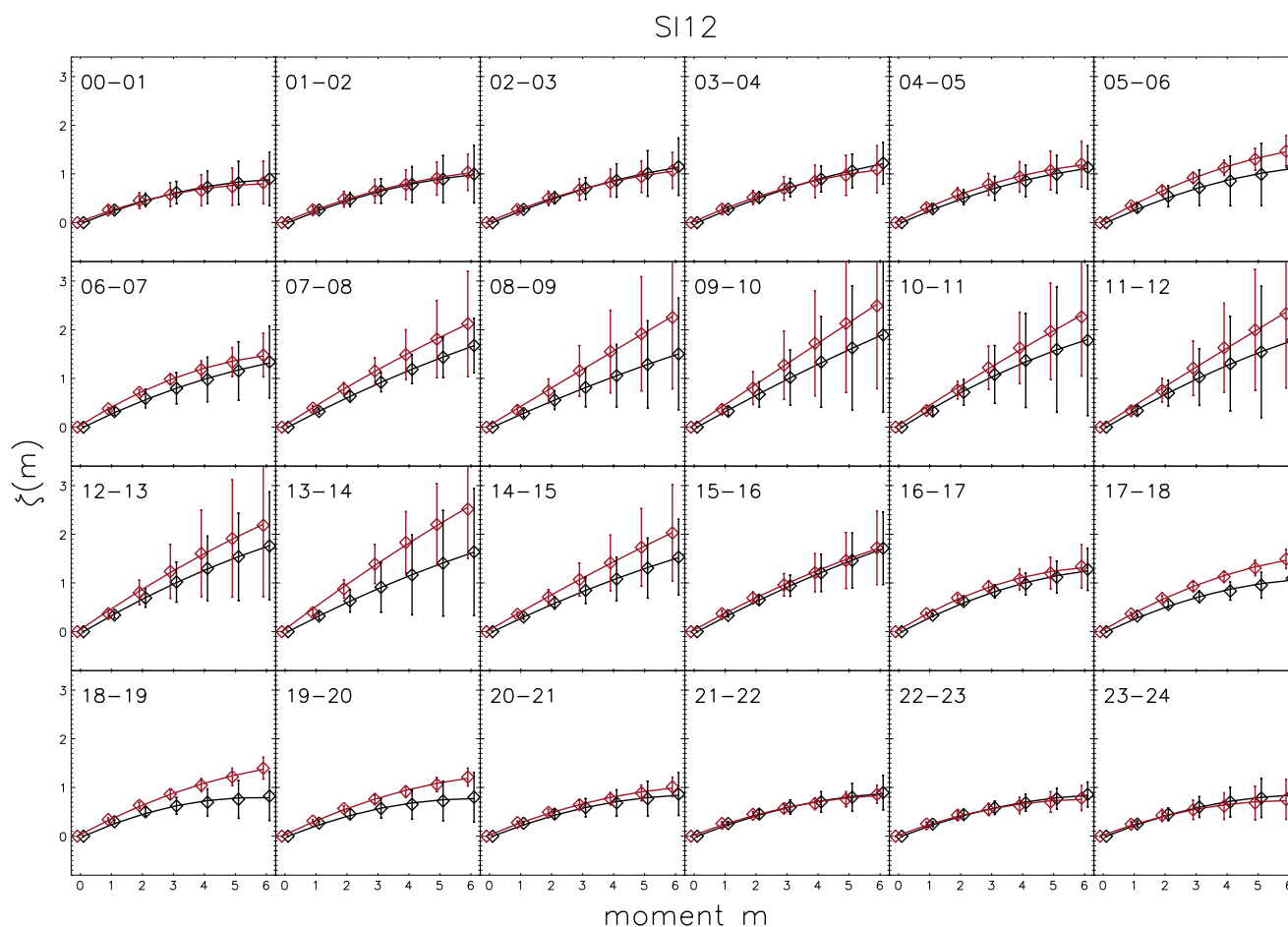
Figure 7. The temporal structure function for moments 1 to 6 ($S_1(\tau)$ to $S_6(\tau)$) of PALB locations derived from the IMAGE SI12 instrument in twenty-four 1 h MLT sectors. Both axes have a logarithmic scale. Structure functions for poleward (positive) boundary motions are shown by the black curves and those for equatorward (negative) boundary motion are shown by red curves. Vertical dashed black lines indicate the 12 to 90 min time separation range.

continuous scale-free dynamics of the dayside PALB motion are not reflected. The dayside characteristics of auroral dynamics are also masked in the dynamic behavior of the geomagnetic indices. This comparison highlights the advantages of investigating the boundary dynamics over a range of MLT sectors.

Differences in the poleward and equatorward motion of the PALB are also evident from the structure function analysis. On the nightside, the poleward PALB structure function exceeds that of the equatorward structure function, implying that the average change in latitude for a particular time scale is greater for poleward motion than for equatorward motion (see equation (1)). This implies that the poleward motion is typically more rapid than the equatorward motion at time separations shorter than the $\tau \approx 90$ min time scale. On the dayside, this relationship is reversed, with the equatorward motion appearing to occur more rapidly. As magnetotail reconnection should drive poleward motion of the OCB while magnetopause reconnection should typically drive equatorward motion of the OCB, the observations in the PALB dynamics are supportive of boundary motion driven by reconnection occurring faster than the undriven relaxation of the boundary toward its equilibrium state after reconnection ends.
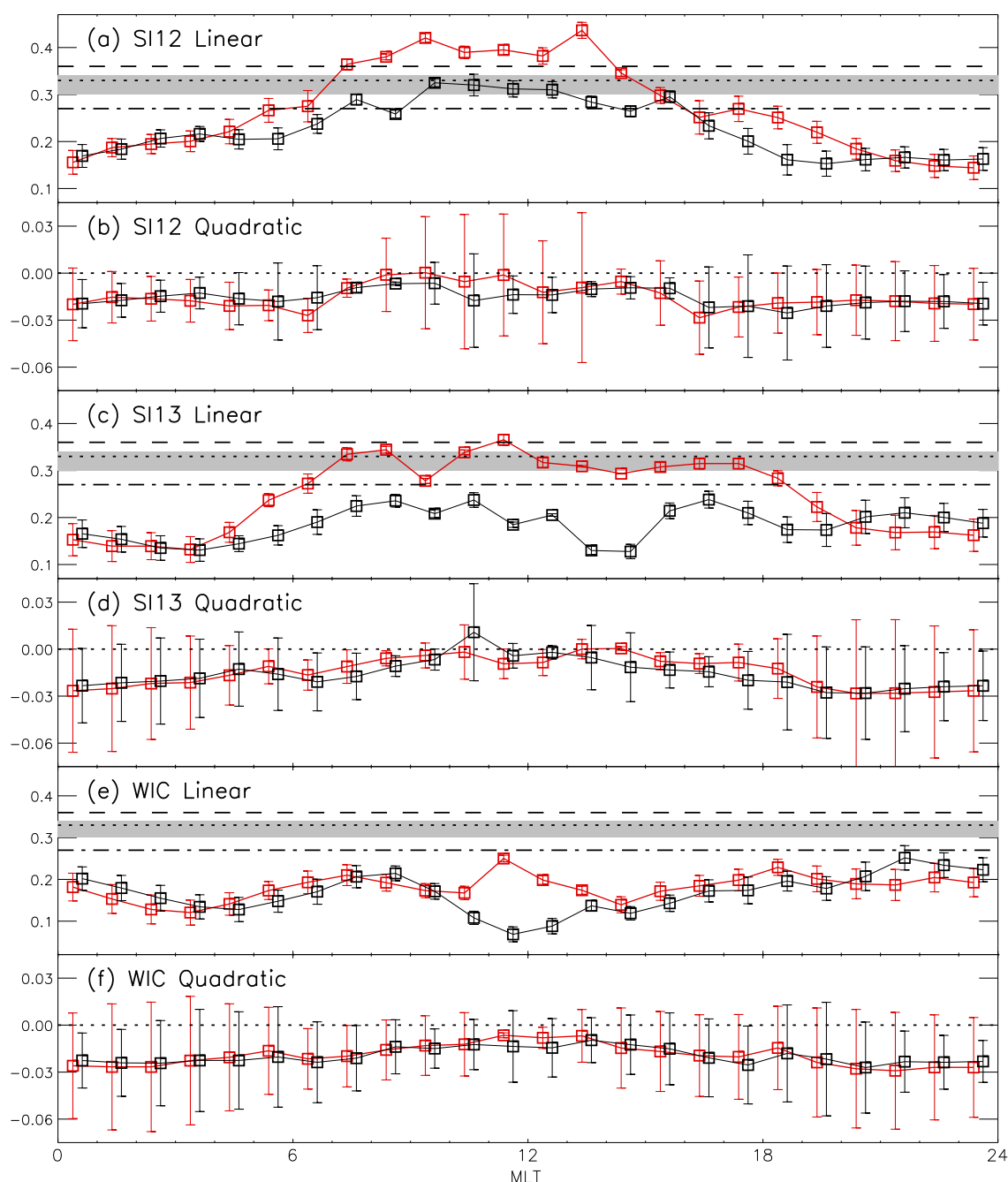
The structure functions of PALB motion at dawn and dusk (Figure 4) show a transition between the dayside and nightside dynamic regimes. This is consistent with the reconfiguration of the auroral boundary and redistribution of open flux around the entire auroral oval following reconnection. From Figure 3, it is clear that the most complex dynamic behavior (lowest structure function value [*Parkinson et al.*, 2007]) is observed around local dawn and dusk on short time separations, reflecting the combined effects of dayside and nightside reconnection. The difference between poleward and equatorward PALB dynamic motion is

Figure 8. The ζ function for moments 0 to 6 of the structure functions for the PALB locations derived from the IMAGE SI12 instrument in twenty-four 1 h MLT sectors. $\zeta(m)$ for poleward (positive) boundary motion is shown by black diamonds and those for equatorward (negative) boundary motion are shown by red diamonds. The best least squares quadratic fits to $\zeta(m)$ are shown for each MLT sector. Error bars show the 95% confidence interval of linear fits to the structure functions shown in Figure 7. The diamond symbols and error bars have been slightly offset with respect to the moment for clarity.

also minimized in the dawn and dusk MLT sectors, further suggesting influence from both magnetopause and magnetotail reconnection.

The scaling break that occurs at large lags ($\sim$ 90 min) in the structure function, predominantly on the night-side, has previously been interpreted as the substorm time scale in the context of auroral indices [e.g., *Takalo et al.*, 1993; *Takalo and Timonen*, 1994; *Takalo et al.*, 1994; *Hnat et al.*, 2003, 2005]. For the auroral boundary motion considered here, we consider a related, more specific interpretation in terms of coupled but unbalanced dayside and nightside magnetic reconnection rates. When dayside reconnection occurs, it opens magnetic flux and causes the OCB to expand equatorward to accommodate this flux, initially locally, then globally, as the perturbation is relaxed around the polar cap boundary [*Freeman and Southwood*, 1988; *Siscoe and Huang*, 1985; *Cowley and Lockwood*, 1992]. The open magnetic flux is carried into the magnetotail where it must be closed by nightside reconnection such that the polar cap boundary does not grow without bound. If dayside reconnection is steady for a time longer than the time scale of the nightside response, then it may be possible for the dayside and nightside reconnection rates to become in balance and the polar cap boundary to be steady. This is the so-called Steady Magnetospheric Convection event [*Sergeev et al.*, 1996]. However, the variability of the solar wind and IMF is such that this is rarely the case. Consequently, on time scales shorter than the response time, we expect the variability of the local polar cap boundary motion within the ionospheric projection of the reconnection sites to dominantly reflect the respective variability of the dayside or nightside reconnection rates. But on longer time scales, we can expect the variability to be bounded.

Figure 9. The variation of the linear and quadratic coefficients of quadratic function fits to the ζ functions with MLT sector. ζ functions relating to structure functions of poleward (positive) PALB motion are shown as solid black curves with square symbols. ζ functions relating to structure functions of equatorward (negative) PALB motion are shown by solid red curves with square symbols. Fit coefficients for ζ functions are shown for (a, b) SI12, (c, d) SI13, and (e, f) WIC PALBs. Error bars show the 95% confidence intervals for the fit to the ζ function. Grey shading in Figures 9a, 9c, and 9e, indicates the slope ($\pm$ uncertainty) of the first-order structure function of the solar wind ϵ parameter calculated during solar maximum by *Hnat et al.* [2005]. The slope of the first-order structure function of the solar wind ϵ parameter calculated during 2000, 2001, and 2002 from *Parkinson et al.* [2007] are shown by the horizontal dotted, dashed, and dash-dotted lines, respectively. The horizontal dotted lines in Figures 9b, 9d, and 9f mark zero. Error bars show the uncertainty of the fitted parameters.

To illustrate the consequences of this on the structure function, we consider a very simple model which superposes two proportional stochastic driving processes with a relative lag between them. These two driving processes represent the contributions to polar cap boundary motion from dayside and nightside reconnection, where the latter is assumed proportional to the former but lagged in time. For simplicity we assume that the drivers are described by ordinary Brownian motion (oBm); this represents a crude
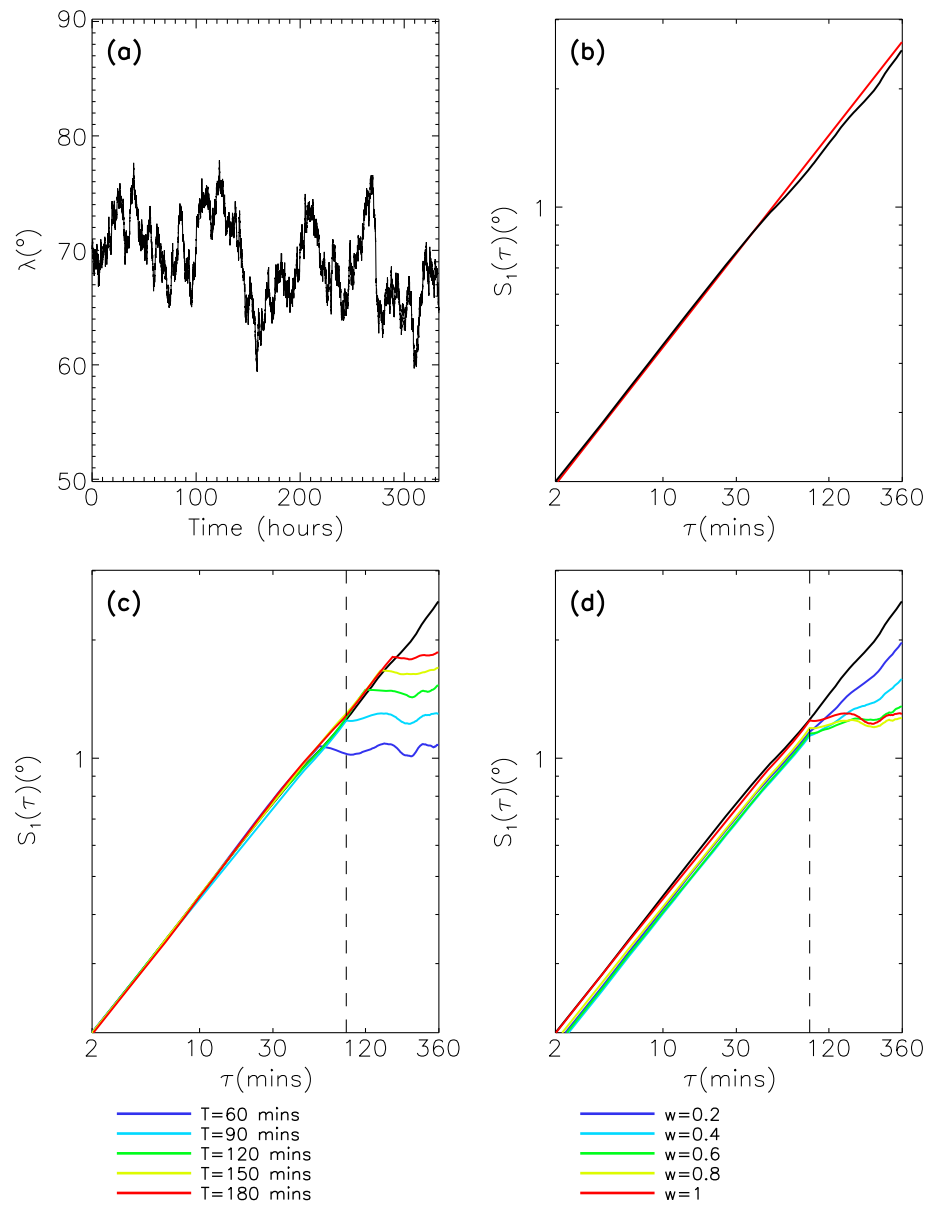
Figure 10. (a) Simulated time series for the PALB location constructed to follow a Brownian random walk. (b) The first-order structure function for the simulated time series (black curve) with the $\tau^{\frac{1}{2}}$ reference structure function for a Brownian random walk (red curve). (c) The first-order structure functions for PALB motion where the motion arises from the superposition of two drivers each following Brownian motion with five different time lags, T, between the drivers. The vertical dashed black line indicates the time separation of 90 min. The black curve is the same structure function as shown in Figure 10b. (d) The first-order structure functions for PALB motion where the motion arises from the superposition of two drivers each following Brownian motion separated by a time lag of 90 min where the relative weighting, w, of one of the drivers varies. The vertical dashed black line indicates the time separation of 90 min. The black curve is the same structure function as shown in Figure 10b.

approximation of the boundary motion but serves to illustrate how the superposition of the two drivers produces the scaling break at large lags.

Figure 10a shows an artificial time series for the PALB location constructed so that the boundary location follows oBm (with mean = 0 and standard deviation = 1) from a starting latitude of 70° and with 2 min time resolution, to simulate a time series derived from IMAGE FUV data. The first-order structure function for this time series should be approximated by $S_1(\tau) =< |\delta\lambda(t,\tau)| >\propto \tau^{\frac{1}{2}}$. Figure 10b shows the first-order structure function calculated for the simulated boundary motion (black line) and the $\tau^{\frac{1}{2}}$ reference curve (red line) for
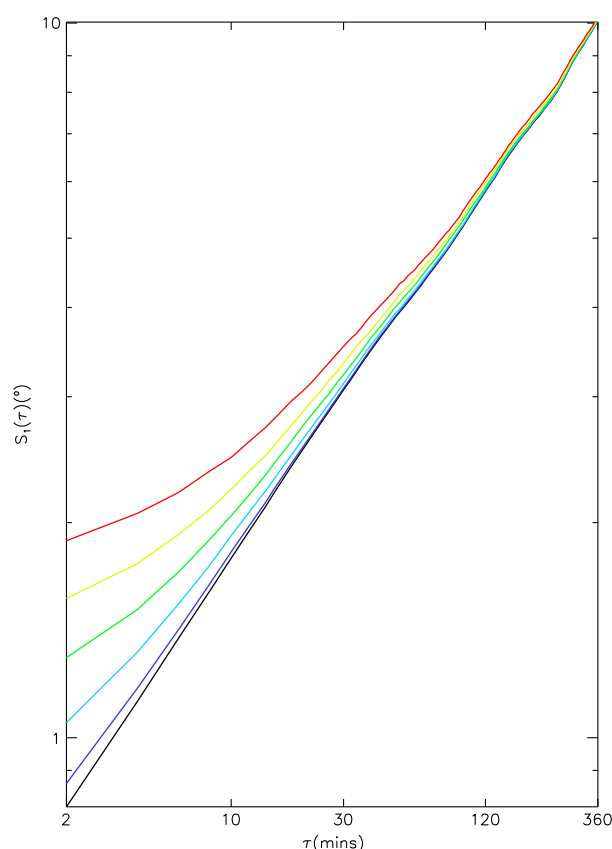
Figure 11. First-order structure functions for a simulated time series for the PALB location constructed to follow a Brownian random walk, with random error in the PALB location. The standard deviation of the random error increases from low (dark blue curve) to high (red curve). No random error has been added to the PALB motion in the structure function shown by the black curve.

the τ range of 2 to 360 min. This represents the situation on the dayside where the boundary motion is dominated by a single-driver, dayside reconnection. Figure 10c shows the first-order structure functions for five sets of PALB motion where this motion is derived from the superposition of two drivers, each following oBm, where the time lag, T, between the drivers, varies. The black curve shows the structure function for PALB motion derived from a single driver following oBm, as shown in Figure 10b, for comparison. For each of the two-driver structure functions, a scaling break is evident where the time separation of the structure function is equal to the time lag between the drivers ($\tau = T$). The vertical dashed black line marks $\tau = 90$ min for comparison with the $T = 90$ min curve (light blue). Figure 10d shows the structure functions for PALB motion derived from the superposition of two drivers following oBm with a time lag between the drivers of 90 min, but where the relative weighting (w) of one of the drivers varies with respect to the other driver. This illustrates the effect of differences in the strength of the reconnection driver between the dayside and the nightside. The red curve ($w = 1$) is equivalent to the light blue curve ($T = 90$ min) in Figure 10c and the black curve again shows the structure function for PALB motion arising from a single oBm driver

from Figure 10b for comparison (this curve is effectively that where $w = 0$). The vertical dashed black line again marks $\tau = 90$ min. A break in scaling at $\tau = T$ is clear for all weights shown; however, the effect of increasing the weighting of the second oBm driver is to reduce the gradient of the structure function following the break until it becomes flat.

This simple modeling suggests that we can interpret the behavior of the PALB motion in the nightside MLT sectors as resulting from the superposition of two competing reconnection drivers; the local reconnection within the magnetotail and the signature of reconnection between the IMF and the dayside magnetopause convecting to the nightside following a time delay. This is consistent with the slope of the structure functions for time separations greater than 90 min flattening in MLT sectors from dusk to the nightside and then increasing again toward dawn (see Figure 4) as the relative importance of the magnetotail reconnection as a driver of the PALB motion varies.

The ζ functions shown in Figure 8 are suggestive of a monofractal regime in the dayside MLT sectors transitioning to a multifractal regime on the nightside. In the multifractal regime, a single scaling exponent cannot be resolved, which has implications for modeling reconnection, as a single stochastic equation would be insufficient to describe the behavior on all time scales. Additionally, scaling exponents derived from linear fits to first-order structure functions in the nightside MLT sectors would be erroneous.

The linear coefficients of the fit to the ζ function for both poleward and equatorward PALB motion from SI12 images in dayside MLT sectors (Figure 9a) are close to those reported by *Hnat et al.* [2005] and *Parkinson et al.* [2007] for the solar wind ϵ parameter for solar maximum and hence the years of our PALB data set. While this could be an indication that the dynamic behavior on the dayside is inherited from the solar wind,

the linear coefficients for the undriven, relaxation motion, where the PALB moves poleward, are closer to the values for the ϵ parameter. However, when PALBs derived from SI13 images are considered, the dynamic behavior of the reconnection-driven equatorward PALB motion more closely resembles that of the solar wind ϵ parameter than the behavior of the undriven, poleward PALB motion, which is highly suggestive of direct inheritance of solar wind dynamic behavior through dayside reconnection. We consider the PALBs derived from WIC images to be less accurate than either SI12 or SI13 in the dayside, as previously detailed.

The scaling break evident at low time separations ($\tau \leq 12$ min) in the structure functions for the dayside MLT sectors could also be inherited from the solar wind; *Hnat et al.* [2005] identified a break in the scaling in the structure function for the ϵ parameter at this time separation during solar minimum. However, the ϵ parameter around solar maximum did not show this break at low time separations and it is evident in the structure functions for PALB motion in most MLT sectors, and for both driven and relaxation motion, making inheritance from the solar wind and IMF an unlikely cause for this scaling break. We suggest another cause for this scaling break. Figure 11 illustrates the effect on the structure function of adding random errors of varying magnitude to a simulated PALB data set. The simulated PALB data set constructed using a single driver following oBm, as shown in Figure 10a, was used as the boundary data set and the structure function for this without added error is shown by the black curve. The colored structure functions are those calculated using this same simulated PALB data set with the addition of random errors with small standard deviation (dark blue curve) to large standard deviation (red curve). The addition of random error reproduces the scaling break observed at low time separations in the data. This random error can be associated with the uncertainty inherent in the PALB determinations. The MLT variation in the scaling at low time separations in Figure 4 can be explained by the greater number of PALBs identified in nightside MLT sectors compared to in the dayside (see Figure 5) and from the differing uncertainty in calculating these boundaries (see *Longden et al.* [2010] for further details).

5. Conclusions

The results of the structure function analysis have highlighted characteristic variations in the dynamic behavior of the PALB:

1. There is clear variation in the dynamic behavior of the PALB with MLT and this variation is obscured when using geomagnetic indices or when combining PALB motions in all MLT sectors.
2. In all MLT sectors, scale-free behavior is evident in PALB fluctuations for time separations greater than 12 min. On the dayside, this scale-free regime extends to at least 360 min, the limit of our structure function analysis. On the nightside, a break in scaling is observed at time separations of ~90 min. We interpret this scaling break as arising from the superposition of the driving motions from reconnection processes from both within the magnetotail and from reconnection between the IMF and dayside magnetopause convecting to the nightside. We consider random errors in the determination of the location of the PALB to be the most likely cause of the departure from scaling observed at short time separations (< 12 min).
3. PALB motion driven by reconnection is typically faster than that attributed to undriven, relaxation processes, with the structure functions for poleward PALB motion in the nightside (driven by magnetotail reconnection) exceeding those of equatorward PALB motion in this time region, while the structure functions for equatorward PALB motion in the dayside (driven by reconnection between the IMF and the magnetopause) exceeding those for poleward motion.
4. Dayside PALB motion is suggestive of a monofractal regime which suggests inheritance from the character of the solar wind and IMF through dayside reconnection. PALB motion on the nightside appears to be multifractal and suggests inheritance from magnetotail processes through reconnection.
5. The dawnside and duskside MLT sectors show the transition between the dayside and nightside characteristics and, frequently, are the MLT sectors showing the most complex behavior.

References

Abel, G. A., M. P. Freeman, and G. Chisham (2006), Spatial structure of ionospheric convection velocities in regions of open and closed magnetic field topology, *Geophys. Res. Lett.*, 33, L24103, doi:10.1029/2006GL027919.

Abel, G. A., M. P. Freeman, G. Chisham, and N. W. Watkins (2007), Investigating turbulent structure of ionospheric plasma velocity using the Halley SuperDARN radar, *Nonlinear Processes Geophys.*, 14, 799–809.

Abel, G. A., M. P. Freeman, and G. Chisham (2009), IMF clock angle control of multifractality in ionospheric velocity fluctuations, *Geophys. Res. Lett.*, 36, L19102, doi:10.1029/2009GL040336.

Akasofu, S.-I., and D. S. Kimball (1965), Auroral morphology as shown by all-sky photographs: Arctic and Antarctic (All-sky photographs to investigate auroral morphology), *Ann. Int. Geophys. Year*, *38*, 299.

Baker, J. B., C. R. Clauer, A. J. Ridley, V. O. Papitashvili, M. J. Brittnacher, and P. T. Newell (2000), The nightside poleward boundary of the auroral oval as seen by DMSP and the ultraviolet imager, *J. Geophys. Res.*, *105*, 21,267–21,280.

Baker, K. B., J. R. Dudeney, R. A. Greenwald, M. Pinnock, P. T. Newell, A. S. Rodger, N. Mattin, and C.-I. Meng (1995), HF radar signatures of the cusp and low-latitude boundary layer, *J. Geophys. Res.*, *100*, 7671–7695.

Baker, K. B., A. S. Rodger, and G. Lu (1997), HF-radar observations of the dayside magnetic merging rate: A Geospace Environment Modeling boundary layer campaign study, *J. Geophys. Res.*, *102*, 9603–9617.

Blanchard, G. T., L. R. Lyons, J. C. Samson, and F. J. Rich (1995), Locating the polar cap boundary from observations of 6300Å auroral emission, *J. Geophys. Res.*, *100*, 7855–7862.

Boakes, P. D., S. E. Milan, G. A. Abel, M. P. Freeman, G. Chisham, B. Hubert, and T. Sotirelis (2008), On the use of IMAGE FUV for estimating the latitude of the open/closed magnetic field line boundary in the ionosphere, *Ann. Geophys.*, *26*, 2759–2769.

Borovsky, J. E. (2008), The rudiments of a theory of solar wind/magnetosphere coupling derived from first principles, *J. Geophys. Res.*, *113*, A08228, doi:10.1029/2007JA012646.

Brittnacher, M., M. Fillingim, G. Parks, G. Germany, and J. Spann (1999), Polar cap area and boundary motion during substorms, *J. Geophys. Res.*, *104*, 12,251–12,262.

Burch, J. L. (2000), IMAGE mission overview, *Space Sci. Rev.*, *91*, 1–14.

Carbary, J. F., T. Sotirelis, P. T. Newell, and C.-I. Meng (2003), Auroral boundary correlations between UVI and DMSP, *J. Geophys. Res.*, *108*(A1), 1018, doi:10.1029/2002JA009378.

Chapman, S. C., B. Hnat, G. Rowlands, and N. W. Watkins (2005), Scaling collapse and structure functions: Identifying self-affinity in finite length time series, *Nonlinear Processes Geophys.*, *12*, 767–774.

Chisham, G., and M. P. Freeman (2003), A technique for accurately determining the cusp-region polar cap boundary using SuperDARN HF radar measurements, *Ann. Geophys.*, *21*, 983–996.

Chisham, G., M. Pinnock, and A. S. Rodger (2001), The response of the HF radar spectral width boundary to a switch in the IMF B_y direction: Ionospheric consequences of transient dayside reconnection?, *J. Geophys. Res.*, *106*, 191–202.

Chisham, G., M. Pinnock, I. J. Coleman, M. R. Hairston, and A. D. M. Walker (2002), An unusual geometry of the ionospheric signature of the cusp: Implications for magnetopause merging sites, *Ann. Geophys.*, *20*, 29–40.

Chisham, G., M. P. Freeman, I. J. Coleman, M. Pinnock, M. R. Hairston, M. Lester, and G. Sofko (2004), Measuring the dayside reconnection rate during an interval of due northward interplanetary magnetic field, *Ann. Geophys.*, *22*, 4243–4258.

Chisham, G., et al. (2008), Remote sensing of the spatial and temporal structure of magnetopause and magnetotail reconnection from the ionosphere, *Rev. Geophys.*, *46*, RG1004, doi:10.1029/2007RG000223.

Cowley, S. W. H., and M. Lockwood (1992), Excitation and decay of solar wind-driven flows in the magnetosphere-ionosphere system, *Ann. Geophys.*, *10*, 103–115.

Feldstein, Y. I., and Yu. I. Galperin (1985), The auroral luminosity structure in the high-latitude upper atmosphere: Its dynamics and relationship to the large-scale structure of the Earth's magnetosphere, *Rev. Geophys.*, *23*, 217–275.

Freeman, M. P., and D. J. Southwood (1988), The effect of magnetospheric erosion on mid- and high-latitude ionospheric flows, *Planet. Space Sci.*, *36*, 509–522.

Freeman, M. P., N. W. Watkins, and D. J. Riley (2000), Evidence for a solar wind origin of the power law burst lifetime distribution of the AE indices, *Geophys. Res. Lett.*, *27*, 1087–1090.

Freeman, M. P., G. Chisham, and I. J. Coleman (2007), Remote sensing of reconnection, in *Reconnection of Magnetic Fields. Magnetohydrodynamics and Collisionless Theory and Observations*, edited by J. Birn and E. Priest, pp. 217–228, Cambridge Univ. Press, Cambridge.

Frey, H. U., S. B. Mende, T. J. Immel, S. A. Fuselier, E. S. Claflin, J.-C. Gérard, and B. Hubert (2002), Proton aurora in the cusp, *J. Geophys. Res.*, *107*(A7), 1091, doi:10.1029/2001JA900161.

Fuselier, S. A., H. U. Frey, K. J. Trattner, S. B. Mende, and J. L. Burch (2002), Cusp aurora dependence on interplanetary magnetic field B_z, *J. Geophys. Res.*, *107*(A7), 1111, doi:10.1029/2001JA900165.

Hnat, B., S. C. Chapman, G. Rowlands, N. W. Watkins, and M. P. Freeman (2003), Scaling in long term data sets of geomagnetic indices and solar wind ϵ as seen by WIND spacecraft, *Geophys. Res. Lett.*, *30*(22), 2174, doi:10.1029/2003GL018209.

Hnat, B., S. C. Chapman, and G. Rowlands (2005), Scaling and a Fokker-Planck model for fluctuations in geomagnetic indices and comparison with solar wind ϵ as seen by Wind and ACE, *J. Geophys. Res.*, *110*, A08206, doi:10.1029/2004JA010824.

Hnat, B., S. C. Chapman, K. Kiyani, G. Rowlands, and N. W. Watkins (2007), On the fractal nature of the magnetic field energy density in the solar wind, *Geophys. Res. Lett.*, *34*, L15108, doi:10.1029/2007GL029531.

Iijima, T., and T. A. Potemra (1978), Large-scale characteristics of field-aligned currents associated with substorms, *J. Geophys. Res.*, *83*, 599–615.

Kauristie, K., J. Weygand, T. I. Pulkkinen, J. S. Murphree, and P. T. Newell (1999), Size of the auroral oval: UV ovals and precipitation boundaries compared, *J. Geophys. Res.*, *104*, 2321–2331.

Kozelov, B. V., V. M. Uritsky, and A. J. Klimas (2004), Power law probability distributions of multiscale auroral dynamics from ground-based TV observations, *Geophys. Res. Lett.*, *31*, L20804, doi:10.1029/2004GL020962.

Longden, N., G. Chisham, M. P. Freeman, G. A. Abel, and T. Sotirelis (2010), Estimating the location of the open-closed magnetic field line boundary from auroral images, *Ann. Geophys.*, *28*, 1659–1678.

Lui, A. T. Y. (2001), Multifractal and intermittent nature of substorm-associated magnetic turbulence in the magnetotail, *J. Atmos. Sol. Terr. Phys.*, *63*, 1379–1385.

Makita, K., and C.-I. Meng (1984), Average electron precipitation patterns and visual aurora characteristics during geomagnetic quiescence, *J. Geophys. Res.*, *89*, 2861–2872.

Makita, K., C.-I. Meng, and S.-I. Akasofu (1983), The shift of the auroral electron precipitation boundaries in the dusk-dawn sector in association with geomagnetic activity and interplanetary magnetic field, *J. Geophys. Res.*, *88*, 7967–7981.

Mende, S. B., et al. (2000a), Far ultraviolet imaging from the IMAGE spacecraft. 1. System design, *Space Sci. Rev.*, *91*, 243–270.

Mende, S. B., et al. (2000b), Far ultraviolet imaging from the IMAGE spacecraft. 2. Wideband FUV imaging, *Space Sci. Rev.*, *91*, 271–285.

Mende, S. B., et al. (2000c), Far ultraviolet imaging from the IMAGE spacecraft. 3. Spectral imaging of the Lyman-α and oi 135.6 nm, *Space Sci. Rev.*, *91*, 287–318.

Milan, S. E., and M. Lester (2001), A classification of spectral populations observed in HF radar backscatter from the E region auroral electrojets, *Ann. Geophys.*, *19*, 189–204.

Milan, S. E., M. Lester, S. W. H. Cowley, J. Moen, P. E. Sandholt, and C. J. Owen (1999), Meridian-scanning photometer, coherent HF radar and magnetometer observations of the cusp: A case study, *Ann. Geophys.*, *17*, 159–172.

Milan, S. E., M. Lester, S. W. H. Cowley, and M. Brittnacher (2000), Convection and auroral response to a southward turning of the IMF: Polar UVI, CUTLASS, and IMAGE signatures of transient magnetic flux transfer at the magnetopause, *J. Geophys. Res.*, *105*, 15,741–15,755.

Milan, S. E., M. Lester, S. W. H. Cowley, K. Oksavik, M. Brittnacher, R. A. Greenwald, G. Sofko, and J.-P. Villain (2003), Variations in the polar cap area during two substorm cycles, *Ann. Geophys.*, *21*, 1121–1140.

Milan, S. E., G. Provan, and B. Hubert (2007), Magnetic flux transport in the Dungey cycle: A survey of dayside and nightside reconnection rates, *J. Geophys. Res.*, *112*, A01209, doi:10.1029/2006JA011642.

Milan, S. E., P. D. Boakes, and B. Hubert (2008), Response of the expanding/contracting polar cap to weak and strong solar wind driving: Implications for substorm onset, *J. Geophys. Res.*, *113*, A09215, doi:10.1029/2008JA013340.

Mishin, V. M. (1990), The magnetogram inversion technique and some applications, *Space Sci. Rev.*, *53*, 83–163.

Mishin, V. M., A. D. Bazarzhapov, T. I. Saifudinova, S. B. Lunyushkin, D. Sh. Shirapov, J. Woch, L. Eliasson, H. Opgenoorth, and J. S. Murphree (1992), Different methods to determine the polar cap area, *J. Geomagn. Geoelec.*, *44*, 1207–1214.

Newell, P. T., W. J. Burke, E. R. Sánchez, C.-I. Meng, M. E. Greenspan, and C. R. Clauer (1991), The low-latitude boundary layer and the boundary plasma sheet at low altitude: Prenoon precipitation regions and convection reversal boundaries, *J. Geophys. Res.*, *96*, 21,013–21,023.

Newell, P. T., Y. I. Feldstein, Y. I. Galperin, and C.-I. Meng (1996), Morphology of nightside precipitation, *J. Geophys. Res.*, *101*, 10,737–10,748.

Parkinson, M. L. (2006), Dynamic critical scaling of electric field fluctuations in the greater cusp and magnetotail implied by HF radar observations of F-region Doppler velocity, *Ann. Geophys.*, *24*, 689–705.

Parkinson, M. L., R. C. Healey, and P. L. Dyson (2007), Solar cycle changes in the geo-effectiveness of small-scale solar wind turbulence measured by Wind and ACE at 1 AU, *Ann. Geophys.*, *25*, 1183–1197.

Sandholt, P. E., C. J. Farrugia, M. Øieroset, P. Stauning, and W. F. Denig (1998), Auroral activity associated with unsteady magnetospheric erosion: Observations on December 18, 1990, *J. Geophys. Res.*, *103*, 2309–2317.

Sergeev, V. A., R. J. Pellinen, and T. I. Pulkkinen (1996), Steady magnetospheric convection: A review of recent results, *Space Sci. Rev.*, *75*, 551–604.

Siscoe, G. L., and T. S. Huang (1985), Polar cap inflation and deflation, *J. Geophys. Res.*, *90*, 543–547.

Sotirelis, T., and P. T. Newell (2000), Boundary-oriented electron precipitation model, *J. Geophys. Res.*, *105*, 18,655–18,673.

Takalo, J., and J. Timonen (1994), Characteristic time scale of auroral electrojet data, *Geophys. Res. Lett.*, *21*, 617–620.

Takalo, J., and J. Timonen (1998), On the relation of the AE and PC indices, *J. Geophys. Res.*, *103*, 29,393–29,398.

Takalo, J., J. Timonen, and H. Koskinen (1993), Correlation dimension and affinity of AE data and bicolored noise, *Geophys. Res. Lett.*, *20*, 1527–1530.

Takalo, J., J. Timonen, and H. Koskinen (1994), Properties of AE data and bicolored noise, *J. Geophys. Res.*, *99*, 13,239–13,249.

Takalo, J., R. Lohikoski, and J. Timonen (1995), Structure function as a tool in AE and Dst time series analysis, *Geophys. Res. Lett.*, *22*, 635–638.

Uritsky, V. M., A. J. Klimas, and D. Vassiliadis (2001), Comparative study of dynamical critical scaling in the auroral electrojet index versus solar wind fluctuations, *Geophys. Res. Lett.*, *28*, 3809–3812.

Uritsky, V. M., A. J. Klimas, D. Vassiliadis, D. Chua, and G. Parks (2002), Scale-free statistics of spatiotemporal auroral emissions as depicted by POLAR UVI images: Dynamic magnetosphere is an avalanching system, *J. Geophys. Res.*, *107*(A12), 1426, doi:10.1029/2001JA000281.

Uritsky, V. M., E. Donovan, A. J. Klimas, and E. Spanswick (2008), Scale-free and scale-dependent modes of energy release dynamics in the nighttime magnetosphere, *Geophys. Res. Lett.*, *35*, L21101, doi:10.1029/2008GL035625.

Vallières-Nollet, M.-A., P. Charbonneau, V. Uritsky, E. Donovan, and W. Liu (2010), Dual scaling for self-organised critical models of the magnetosphere, *J. Geophys. Res.*, *115*, A12217, doi:10.1029/2010JA015641.

Vampola, A. L. (1971), Access of solar electrons to closed field lines, *J. Geophys. Res.*, *76*, 36–43.

Vörös, Z., P. Kovács, A. Juhász, A. Körmendi, and A. W. Green (1998), Scaling laws from geomagnetic time series, *Geophys. Res. Lett.*, *25*, 2621–2624.

Vörös, Z., et al. (2003), Multi-scale magnetic field intermittence in the plasma sheet, *Ann. Geophys.*, *21*, 1955–1964.

Wanliss, J. A. (2005), Fractal properties of SYM-H during quiet and active times, *J. Geophys. Res.*, *110*, A03202, doi:10.1029/2004JA010544.

Watkins, N. W. (2002), Scaling in the space climatology of the auroral indices: Is SOC the only possible description?, *Nonlinear Processes Geophys.*, *9*, 389–397.

Wild, J. A., S. E. Milan, C. J. Owen, J. M. Bosqued, M. Lester, D. M. Wright, H. Frey, C. W. Carlson, A. N. Fazakerley, and H. Rème (2004), The location of the open-closed magnetic field line boundary in the dawn sector auroral ionosphere, *Ann. Geophys.*, *22*, 3625–3639.